Uncovering Buried Structure and Interfaces in Molecular Photovoltaics

James B. Gilchrist, Toby. H. Basey-Fisher, Sharon C'E. Chang, Frank Scheltens, David W. McComb, and Sandrine Heutz**

The processes that generate current in organic photovoltaics are highly dependent on the micro- and nano-structure in the semiconductor layers, especially at the donor-acceptor interface. Elucidating film properties throughout the thickness of the devices is therefore key to their further development. Here, a methodology is developed to gain unprecedented insights into the structure and composition of the molecular layers within the depth of device structure using high resolution transmission electron microscopy (HRTEM). The technique was applied to three archetypical solar cell configurations consisting of copper phthalocyanine (CuPc) and C_{60}, which have been cross-sectioned using a focused ion beam method optimized to minimize sample damage. The HRTEM images exhibit lattice fringes in both CuPc and C_{60}, confirming the crystallinity and texture of both materials, and offering novel insight into the growth of C_{60} onto molecular materials. The donor-acceptor interface morphology is further studied using scanning transmission electron microscopy (STEM) in combination with energy dispersive X-ray (EDX) spectroscopy, extending the scope of our methodology to amorphous heterostructures.

1. Introduction

The active layer of organic solar cell devices consists of a thin film composed of different materials in which processes such as exciton generation and diffusion, charge dissociation at a donor-acceptor interface and charge transport occur.[1–4] The thickness of these films depends on the exciton diffusion length and device architecture and can vary from tens to hundreds of nanometers.[5–7] Provided that the generated charges can be collected at suitable contacts the solar cell device can be used as a source of electrical power. The advantages of using organic materials (lightweight, flexible, low-cost, etc.) for photovoltaic devices have been professed for many years.[8–11] Currently, efficiencies for laboratory-scale devices are in the range of 5 – 10% with further increases expected.[7,12–14] Different methods for achieving optimization are being pursued based on developing new molecules[14] and device structures[3,15] or controlling physical properties, e.g., morphology or crystal and electronic structure.[7,12,16] These strategies rely on an understanding of the donor-acceptor interface and film properties within the device. Many techniques have been developed to assess this buried structure such as ellipsometry,[17] X-ray scattering[18–20] and reflectivity,[21] neutron scattering[22] and reflectometry,[23] a combination of X-ray and atomic force microscopies,[24,25] X-ray spectroscopy[26] and secondary ion mass spectrometry.[19,27] However, such techniques probe the bulk of the device and higher spatial resolution techniques are important to gain insight on the molecular scale.

Organic materials have been studied extensively using transmission electron microscopy (TEM), and the observation of lattice fringes in crystalline regions has been widely reported.[28–30] For the case of some phthalocyanines, individual molecules have even been resolved,[31] and more recently, sub-molecular structure has been observed in the more electron beam stable chlorinated copper phthalocyanine using aberration corrected scanning transmission electron microscopy (STEM) methods.[32,33]

TEM and its associated spectroscopies can be applied to the study of buried structure if electron transparent cross-sections can be prepared. Cross-sections of organic materials have been obtained previously using techniques such as ultramicrotomy and ion beam milling.[34] It has been shown that the crystallinity of organic films can be preserved in cross-sections of films on hard substrates using argon ion milling.[35] Site specific cross-sections can be prepared using dual-beam instruments, where a scanning electron microscope (SEM) is combined with a

J. B. Gilchrist, Dr. T. H. Basey-Fisher, Dr. S. Heutz
Department of Materials
Imperial College London
SW7 2AZ, UK
E-mail: s.heutz@imperial.ac.uk
S. C'E. Chang
Department of Physics and Graduate School for Integrative Sciences and Engineering
National University of Singapore
Singapore and Department of Materials
Imperial College London
SW7 2AZ, UK
Dr. F. Scheltens, Prof. D. W. McComb
Department of Material Science and Engineering
The Ohio State University
Columbus, Ohio 43212, USA
E-mail: mccomb.29@osu.edu

DOI: 10.1002/adfm.201400345

focused ion beam (FIB).[36] TEM sample preparation using such instruments is common for inorganic materials but less so for organic systems as the ion beam may cause significant damage, considerably complicating the interpretation of images.

Work has previously been performed on minimizing FIB damage in materials by reducing the accelerating voltage and the beam current (by selecting a smaller beam defining aperture) *i.e.* reducing the kinetic energy of the ions and total flux. This is measured by the reduction of the amorphous regions in FIB prepared samples of crystalline materials with lower accelerating voltages.[37–39]

For hybrid solar cells, where the active layer is composed of both organic and inorganic materials, the large difference in scattering cross-section can provide substantial contrast between the materials of interest when performing TEM imaging.[40] However for purely organic systems, where the scattering cross-sections and densities are similar, identification of the different components and interfaces between them can be challenging, despite some promising results in small molecule-polymer blends.[41] To date, preparation of device cross-sections that can be used to obtain information on crystallinity, molecular orientation, and interface morphology on the nanometer scale has been largely unsuccessful.

In this contribution we show that cross-sections of unprecedented quality can be obtained in molecular heterostructures of copper phthalocyanine (CuPc) and C_{60}. CuPc has been well characterized using bulk diffraction techniques, where different structures and textures have been identified and correlated to device efficiencies.[16,29,42,43] Films of C_{60} are less well understood, with some previous work detailing their crystalline nature.[44–46] Our HRTEM results demonstrate that an optimized thinning procedure using a FIB enables the preparation of cross-sections which retain their crystalline nature and give novel information about texture in molecular films. Material identification can be performed using phase contrast within the crystalline regions of the organic films in idealized structures, but becomes problematic on actual device structures which are structurally more disorganized. For the first time we demonstrate that energy dispersive X-ray spectroscopy (EDX) performed in the STEM can be used to differentiate materials in organic heterojunction device cross-sections based on their elemental composition. This is possible due to improved high brightness electron sources and developments in EDX detector technology (silicon drift detectors) that results in increased solid angle and detector efficiencies that make faster acquisition of statistically reliable data possible and permit mapping of even low atomic number elements.[47]

2. Results and Discussion

The in situ lift-out technique using FIB milling is a widely used procedure for preparation of cross-sectional TEM specimens.[48] We have modified the standard protocols in order to minimize the energy transfer from ion implantation in the TEM foil. Minimizing this energy transfer is key to obtaining cross-sections of organic films without completely amorphizing the material. This has been achieved by reducing the accelerating voltage to 1 kV and the beam current to 5.3 pA for the final thinning, as well as reducing the angle that the beam makes with the lamella to 0.2°.

We have applied the optimised cross-sectioning method to three archetypical solar cell systems based on CuPc and C_{60} (**Figure 1**a-c). The different architectures have been chosen as they represent strategies that have been previously used to improve device performance by microstructure engineering.[16,49] The structures were grown both on silicon, which provides sharper interfaces for fundamental study, and on indium tin oxide (ITO), which is more representative of an actual device.

2.1. HRTEM Analysis of Organic Solar Cell Cross-Sections

2.1.1. Bi-layer Structure Grown on Silicon

Figure 2a is a high resolution transmission electron microscope (HRTEM) image of a cross-section of the bi-layer structure grown on silicon. For the first time, lattice fringes are observed both in the CuPc and C_{60} films in cross-section. This exciting result demonstrates that our optimized FIB preparation protocol can provide specimens which, when imaged, retain features corresponding to the known crystal structure. Although a thin amorphized layer is expected to be present on either face of the foil, it has minimal effect on the experimental data.

In the CuPc film the fringes are generally oriented parallel to the substrate surface and have a spacing of 1.3 nm (Figure 2b). These are formed by diffraction from the (100) plane of the

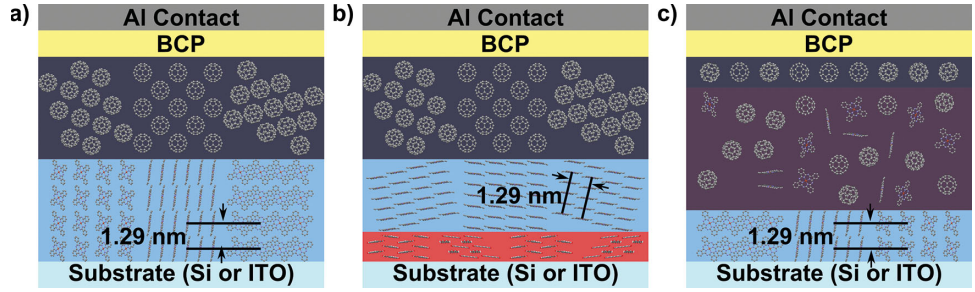

Figure 1. Schematic cross-sectional diagrams, not to scale, for the three solar cell structures studied. a) The bi-layer comprises films of 30 nm CuPc (light blue) and 40 nm C_{60} (dark blue). b) The templated bi-layer comprises 5 nm PTCDA (red), 30 nm CuPc and 40 nm C_{60}. c) The bulk-heterojunction is composed of 3.5 nm CuPc, 50 nm mixed film (ratio 1:1) (purple) and 5 nm C_{60}. The CuPc (100) plane spacing and its orientation are shown in the CuPc film of each device. All structures also contain a 12 nm BCP and a 100 nm Al layer on top of the C_{60}.

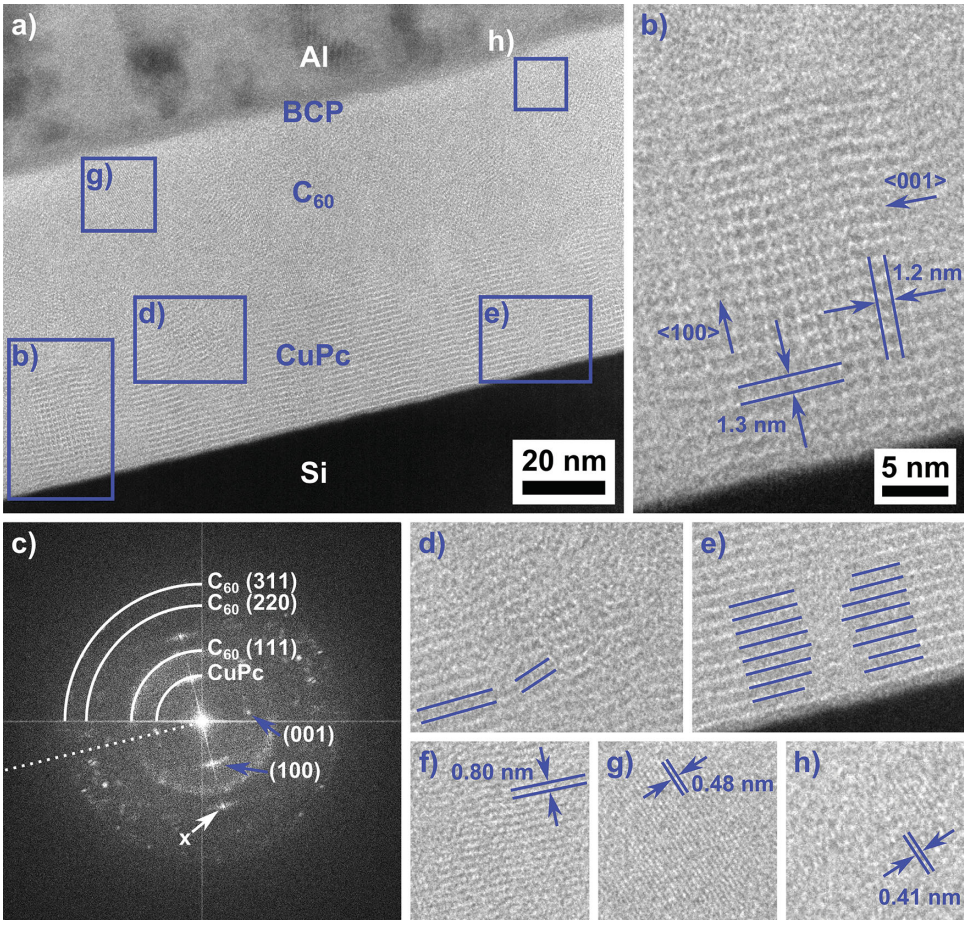

Figure 2. a) HRTEM image of a cross-section of the bi-layer solar cell structure grown on silicon. The different layers can be identified by the varying contrast in the image. b) Detail of regions in (a) showing the CuPc (100) and (001) fringes with spacings of 1.3 and 1.2 nm respectively. c) FFT of (a) displaying the main spatial frequencies found in the image with the CuPc (100) and (001) highlighted by blue arrows. The white dotted line shows the relative orientation of the substrate surface. The feature highlighed with the white arrow corresponds to spacings consistent with the C_{60} (200) plane, but arises mainly at the interface with the substrate. As it does not correspond to any CuPc spacing, it cannot at present be indexed. d) Region where the orientation of the (100) fringes deviates from parallel to the substrate surface. e) Features showing the discontinuities in the CuPc (100) fringes. Fringes observed in the C_{60} film identified as arising from diffraction from the f) (111), g) (220) and h) (311) lattice planes. Note that the C_{60} (111) lattice fringe shown in (f) is from another image taken from the same cross-section under the same conditions.

α-phase CuPc as indexed by Hoshino et al., with corresponding interplanar spacing, d, of 1.29 nm, which is typical of CuPc film growth at room temperature on weakly interacting substrates.[50] The orientation of the lattice fringes parallel to the substrate also corresponds well with texture measurements performed by X-ray diffraction (XRD) and electron paramagnetic resonance (EPR).[51]

A fast Fourier transform (FFT) of an HRTEM image is a convenient way to explore the angular relationship between different spatial frequencies in an image (Figure 2c). The frequencies arising from the CuPc (100) lattice fringes are oriented perpendicular to the substrate surface (the relative orientation of which is marked as the white dotted line). Some regions exhibit additional fringes oriented perpendicular to the CuPc (100) fringes, with a spacing of 1.2 nm (Figure 2b) These are attributed to the CuPc (001) plane (d = 1.20 nm) and are observed in the FFT as intensity perpendicular to the CuPc (100) intensity. Since the lattice spacings are relatively similar, the peaks from both the CuPc (100) and (001) are located at similar distances from the center of the FFT. The co-existence of perpendicular (100) and (001) lattice fringes in regions of the film is explained by CuPc grains being textured with respect to the substrate normal, but randomly oriented in the substrate plane. In an orientation where both the (100) and (001) fringes are observed, the electron beam is close to parallel to the axis of molecular stacking (b-axis), as shown previously in top-view TEM analyses.[29]

Although the (100) fringes are predominantly oriented parallel to the substrate surface, there are regions where the fringes are tilted with respect to adjacent fringes (Figure 2d). It is possible that these fringes are due to a grain growing in a slightly modified orientation or crystal defects, which are commonly observed in similar organic crystals.[28,52–55] The presence of alternative crystal orientations is supported by the observation of the loss of texture in thicker films observed by XRD.[29]

Further examination reveals the CuPc (100) fringes are not continuous throughout the film (Figure 2e). Regions where the fringes are absent are surrounded on each side with regions

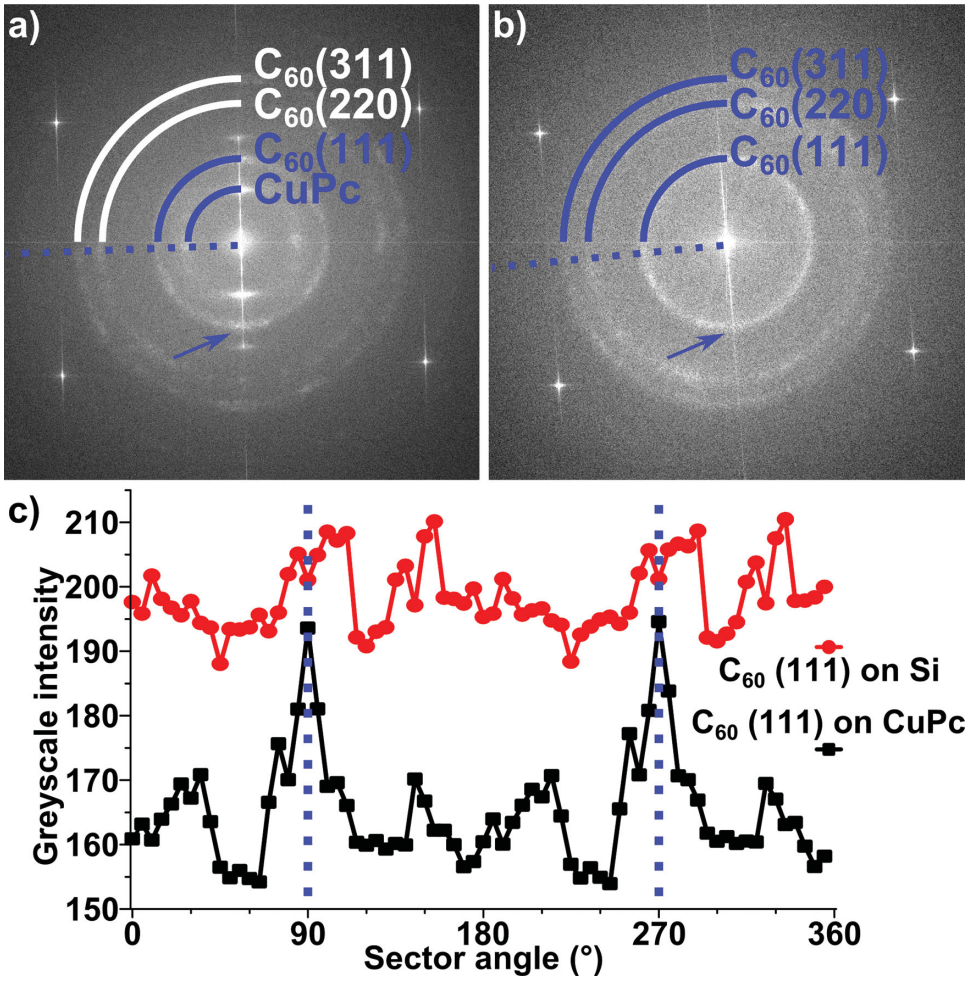

Figure 3. a) Averaged FFT with arrows indicating the frequency from the C_{60} (111) lattice fringe is more intense when in line with the CuPc/C_{60} interface compared to other orientations in the the bi-layer structure. b) This effect is not observed in similar FFTs of a 40 nm C_{60} film grown directly on silicon. c) Graph showing the angular variation in average intensity calculated from a 5° sector spanning the frequency corresponding to the C_{60} (111) lattice fringe. 0° represents the orientation parallel to the substrate surface, peaks can clearly be observed at 90° and 270° i.e. perpendicular to the substrate surface. These peaks are not observed when C_{60} is grown directly on silicon.

of fringes that are aligned with each other, suggesting that the crystal orientation is unchanged with respect to the (100) plane. Although this could be evidence for structural disruption at grain boundaries, distinguishing these features from artifacts introduced during the sample preparation, such as curtaining,[56–59] is challenging.

Three distinct fringe spacings can be identified in the C_{60} film, measuring 0.80 nm, 0.48 nm and 0.41 nm (Figure 2f, g and h, respectively). Based on the structure proposed by Dorset and McCourt,[60] these fringes are attributed to the (111), (220) and (311) planes, respectively. Although the (111) fringes have been observed previously in samples investigated in top view[46,61] and in C_{60} rods,[62] the higher order lattice fringes have to our knowledge never previously been observed in HRTEM images. All mentioned planes have been identified previously using XRD, on thicker films[45] and those of a comparable thickness,[46] and correspond closely to the spacings observed in our TEM cross-sections.

Throughout the cross-section the C_{60} (111) fringes appear to show a slightly preferred orientation which is parallel to the CuPc/C_{60} interface. Although this orientation preference can be observed in individual images and FFTs, the effect can be enhanced by averaging a series of FFTs obtained from images recorded at different regions of the same cross-section under identical conditions. The C_{60} (111) peaks display increased intensity when perpendicular to the substrate surface, the CuPc (100) fringes and the CuPc/C_{60} interface (**Figure 3**a and c). This preferential orientation is not seen in the FFTs of cross-sections of purely C_{60} films grown directly onto silicon (Figure 3b and c), confirming this is solely due to the presence of the underlying CuPc layer. The intensity changes observed elsewhere in the C_{60} (111) frequency are likely due to noise, since the changes observed are similar in scale to those observed single layer structure.

2.1.2. Templated Bi-Layer Structure Grown on Silicon

Growth of CuPc films on 3,4,9,10-perylene tetracarboxylic dianhydride (PTCDA) has been known to change the orientation

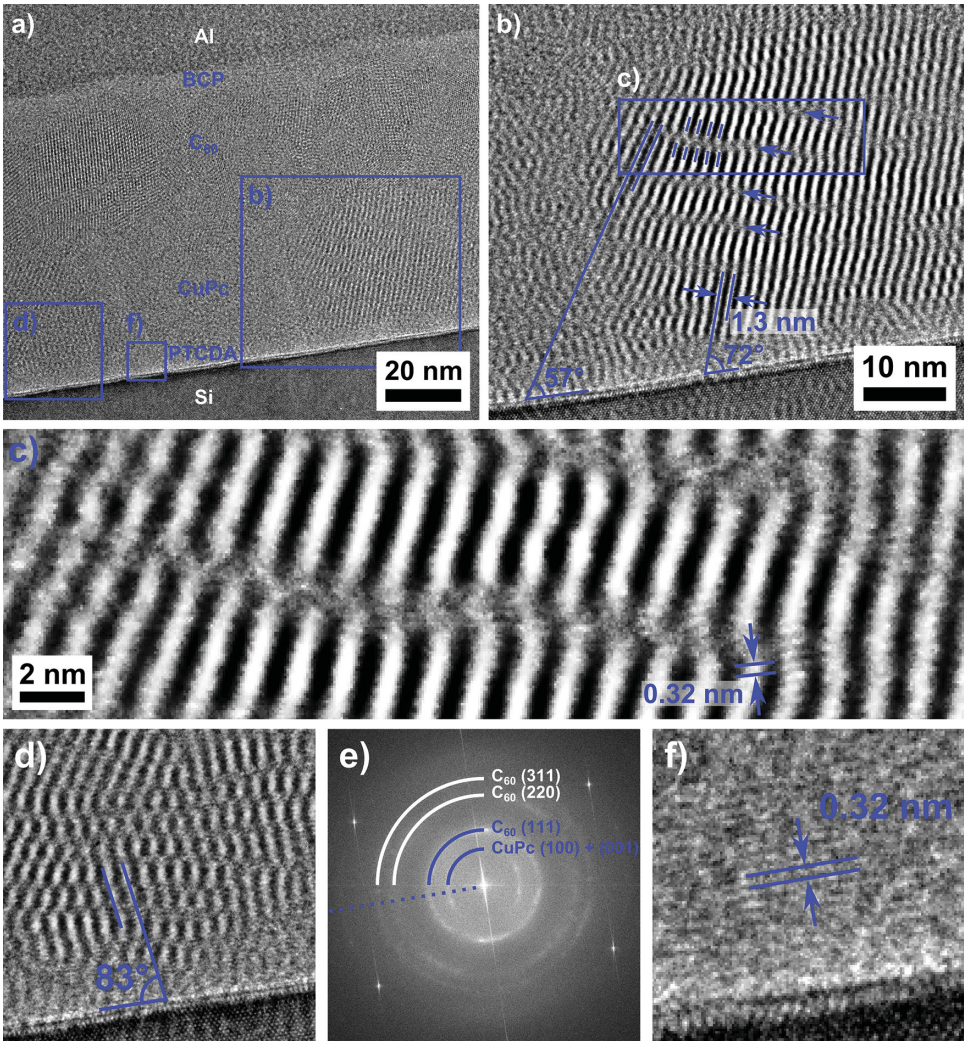

Figure 4. a) HRTEM image of a cross-section of the templated bi-layer structure grown on silicon. b) HRTEM image in which the CuPc (100) lattice fringes have been enhanced by Fourier filtering, where the CuPc fringes are observed at angles of 72° and 57° to the substrate surface. The arrows indicate the regions where disorder in the molecular stacking direction occurs. Fringes either side of these regions are misaligned by about 0.47 nm. c) The disordered regions are about 1 nm thick. Fringes with a spacing of 0.32 nm oriented close to parallel to the substrate surface suggest the (11–2) lattice plane. d) CuPc fringes at 83° to the substrate surface, which are likely to arise from (100) planes. e) Averaged FFT with corresponding substrate surface orientation, depicted by the dotted line. f) Faint fringes at the silicon/organic interface, where the PTCDA film is located. The spacing of these fringes suggests the PTCDA (10–2) plane.

of the molecular structure with respect to the substrate.[16] The phthalocyanine molecules are oriented close to parallel to the substrate surface in a process referred to as "templating".[51,63,64] Since charge transport and photon absorption within CuPc are anisotropic and more favorable when the molecules are parallel to the substrate, this orientation results in improved performance in photovoltaic devices (Figure 1b).[15,16]

HRTEM images of cross-sections of solar cell structures where the CuPc film has been templated using PTCDA reveal that fringes in the CuPc film are not parallel to the substrate surface (**Figure 4**a). Instead the fringes are oriented at angles ranging between 57 and 90° to the substrate surface, with the most common angle being in the range of 70–72°. Powder XRD patterns (θ-2θ mode) show that the most intense peak arises from diffraction from the CuPc (11–2) plane, which is close to parallel to the substrate surface, as confirmed by texture analysis and EPR studies.[29,51] This corresponds to CuPc (100) planes oriented at 75° with respect to the substrate – in good agreement with HRTEM data (Figure 4b).

Within the crystalline grain of CuPc in Figure 4b, there are regions in which the CuPc (100) fringes are less visible. These regions, highlighted by arrows, lie close to perpendicular to the surrounding fringes. The fringes either side of these regions do not align with one another, which might suggest the occurrence of a stacking fault, again observed in similar organic systems.[28,52–55] Indeed, changes in the stacking direction of CuPc molecules disrupt the phase change that the electron beam undergoes as it is transmitted through the foil, reducing visibility of the lattice fringes. The size of the featureless regions (~1 nm in width) suggests that the disruption in the stacking extends over several CuPc molecules. A simple schematic for stacking faults is given in the Supplementary Information;

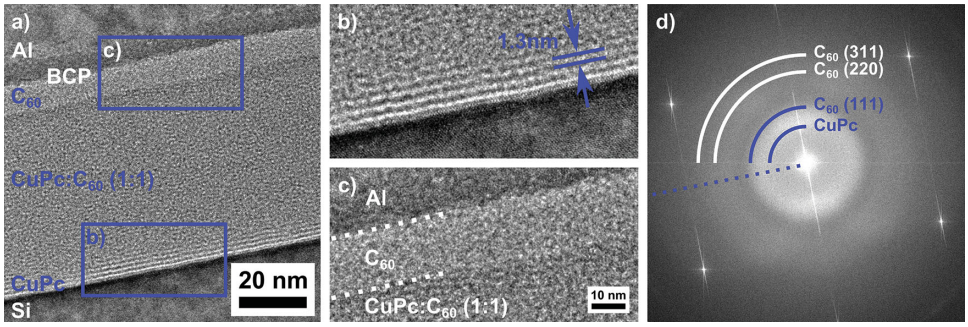

Figure 5. a) HRTEM image of a cross-section of the bulk-heterojunction structure grown on silicon, where no fringes are observed in the mixed film. b) CuPc (100) fringes observed in the pure film. c) No fringes observed in the C_{60} pure film. d) Averaged FFT confirming the absence of spatial frequencies at the expected spacings for C_{60}.

image simulations would be required for a more detailed interpretation of the fault in three dimensions.

On close inspection of the same CuPc grain shown in Figure 4b, fringes with a spacing 0.32 nm can be observed (Figure 4c). The spacing and orientation with respect to the substrate surface (*i.e.* close to parallel) suggest the fringes arise from diffraction from the CuPc (11–2) lattice plane, again confirming the molecular orientation with respect to the substrate. XRD shows that the CuPc (01–2) plane is also parallel to the substrate surface. When in this orientation, the CuPc (100) planes are oriented at 90° to the substrate surface. The CuPc (001) plane, as seen in the previous section, can also be imaged using HRTEM in cross-section. In the two orientations described, the (001) fringes should make an angle of 63° and 64° to the substrate surface.

As well as fringes being observed at all orientations expected from previous XRD analysis,[29] unexpected angles relative to the substrate surface are also observed, Figure 4b and d show examples of fringes oriented at 57° and 83°. The range of orientations can be seen clearly in an FFT, made by averaging a series of FFTs from regions of the same cross-section (Figure 4e). This shows intensity due to the (001) and (100) lattice fringes over the angular range of ~60° to 90° to the substrate surface.

Focusing on the silicon/organic interface region, corresponding to the PTCDA film, fringes parallel on the substrate surface with a spacing of 0.32 nm can be observed (Figure 4f). This is consistent with results from XRD[42] and can be indexed as the (10–2) plane from β-PTCDA structure proposed by Tojo and Mizuguchi.[65] In this configuration, the PTCDA molecules lie close to parallel to the substrate surface, suggesting that templating occurs via π–π interactions between PTCDA and CuPc.

The effect of the templated CuPc layer on the C_{60} fringe orientation appears to be present in these heterostructures. In the averaged FFT (Figure 4e) the frequency corresponding to the C_{60} (111) fringe shows a slight increase in intensity when perpendicular to the substrate surface and CuPc/C_{60} interface. Since it has been established that the substrate does not have an effect on the C_{60} crystal orientation, this confirms that the C_{60} preferential orientation is due to growth onto CuPc.

2.1.3. Bulk-heterojunction Structure Grown on Silicon

In order to improve performance in photovoltaic devices, 'bulk-heterojunction' structures are typically used for organic solar cells. This involves making an active layer film with a large interfacial area by intimately mixing donor and acceptor materials. A schematic of the device structure containing the mixed layer sandwiched between pure films of CuPc and C_{60} is shown in Figure 1c. In cross-sectional images the pure CuPc film, 3.5 nm thick, grown directly on the substrate, can be identified from the CuPc (100) fringes (**Figure 5**a and b). In the 50 nm thick mixed film layer there are no fringes observed, which suggests no crystalline aggregates are present, or that any crystalline aggregates are too small to be identified within the thickness of the foil. This is correlated with the absence of any reflections from XRD and recent EPR studies.[51]

The 5 nm thick pure C_{60} film, grown on the co-deposited layer, is identified by the lighter region in the cross sectional image and exhibits no lattice fringes (Figure 5c). Along with the templating effect on C_{60} crystal orientation in the bi-layer structures this highlights that the microstructure of crystalline C_{60} films depends on the surface on which it is being grown. The FFT of the image is included (Figure 5d) confirming there are no spatial frequencies in the expected positions for the C_{60} lattice in the image. The frequency arising from the CuPc (100) fringe is not obvious in the FFT when compared to the bi-layer system, because only a small proportion of the image contains the frequency.

2.1.4. Device Structures Grown on ITO

We have demonstrated that our TEM sample preparation technique preserves the crystallinity in cross-sections of organic heterostructures on silicon substrates, and that HRTEM gives access to new information that was not available from XRD techniques. The procedure is now extended to the samples grown on the ITO substrates used for device fabrication.

The cross-sectional images of samples grown on ITO (**Figure 6**) are similar to those grown on silicon but the increased roughness of the ITO/organic interface makes the interpretation more complex.

In the bi-layer structure, CuPc and C_{60} fringes are observed with the same spacings as on silicon substrates (Figure 6a). A greater range in orientation of the CuPc fringes is observed (Figure 6b), but, as highlighted in the image and in the FFT (Figure 6c), the CuPc fringes predominately lie parallel to the substrate surface.

The FFT reveals that the C_{60} (111) fringe does not display a preferred orientation with respect to the CuPc (100) fringe, in contrast to the bi-layer samples grown on silicon. This may be a result of the wider distribution of CuPc orientations, which renders the templating ineffective.

In the templated bi-layer structure on ITO, the CuPc (100) fringes are observed at angles of about 60° to the ITO surface (Figure 6d and e), similar to the equivalent structure on silicon, which suggests that the PTCDA templating is still effective, as seen from XRD.[16] But, as observed in the bi-layer structure above, there is a wider range of orientations of these fringes, shown in the FFT (Figure 6f). The bulk-heterojunction structure on ITO displays no CuPc fringes at the ITO/CuPc interface (Figure 6g). It could be expected that the characteristic crystalline fringes of the pure CuPc film might not be observed due to the thin nature of this film and the comparably large roughness of the ITO surface. This roughness, when projected through the thickness of the foil could obscure the expected fringes. There are, however, very faint fringes in the pure C_{60} film with a spacing of 0.51 nm, which corresponds closely to the C_{60} (220). As seen with the bi-layer structure, crystalline C_{60} appears to be highly dependent on the surface which it is grown.

2.2. Energy Dispersive X-ray (EDX) Analysis of Organic Solar Cell Cross-Sections

The prominent fringes observed when the structures are grown on silicon provide a direct method to identify films and the relative crystallographic orientation of CuPc and C_{60}. However, the basic position and structure of the donor-acceptor interface can be difficult to identify in cross-sectional HRTEM images of the simplified device structures grown on silicon. The complexity is further increased when these structures are grown on the conventionally used transparent electrode ITO. There is therefore a need for a method that is able to identify the donor and acceptor materials in order to distinguish and further probe the technologically relevant donor-acceptor interface.

STEM-EDX analysis can be used to distinguish regions of electron transparent foils via elemental composition with a high spatial resolution. This is often done by sequential acquisition of spectra over the region of interest to form a three-dimensional data set referred to as a spectrum image. The local composition can be calculated using the ratio of X-ray intensities emitted by different elements in the specimen in individual spectra (Equation (1)).[66]

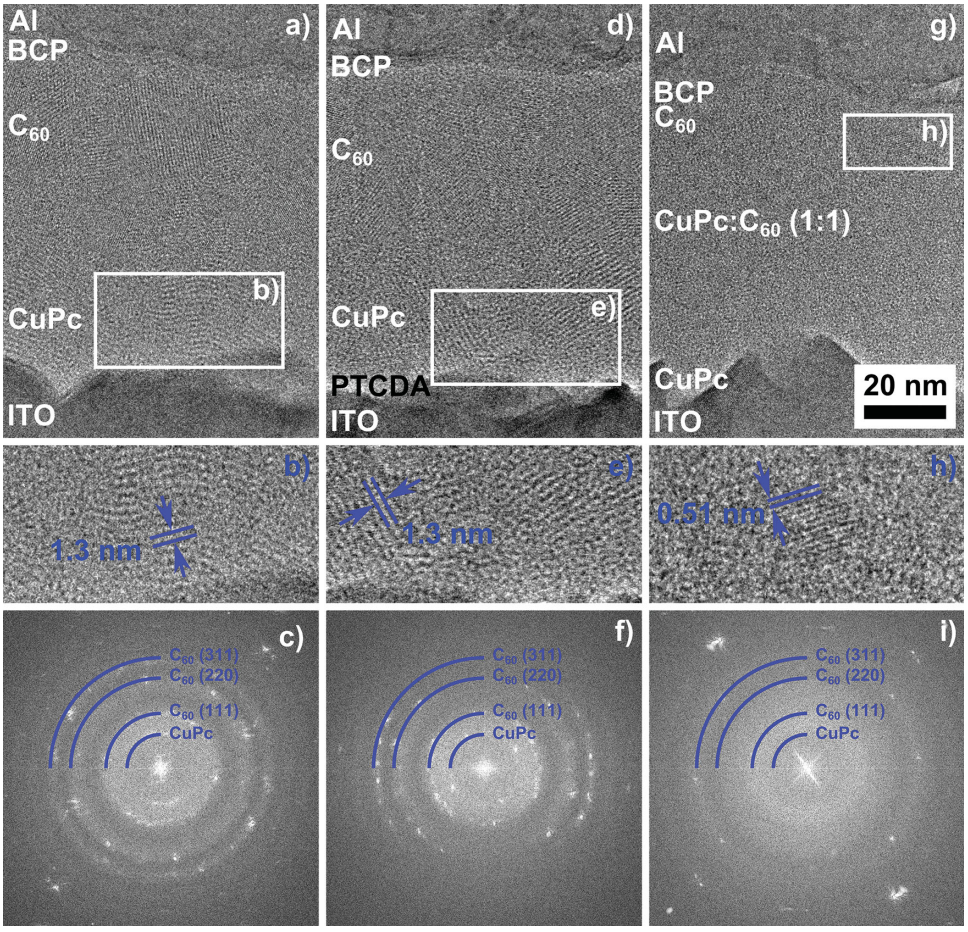

Figure 6. HRTEM images of cross-sections of the three solar cell structures grown on ITO. a) The bi-layer structure, with b) showing a detail of the CuPc (100) fringes. c) FFT of (a). d) The templated bi-layer structure, with e) the CuPc (100) fringes oriented at various angles to the surface. f) FFT of (d). g) The bulk-heterojunction structure with the C_{60} (220) fringes highlighted in (h). i) FFT of (g). In all FFTs, spatial frequencies higher than the C_{60} (311) spacing arise from the ITO substrate or detector noise.

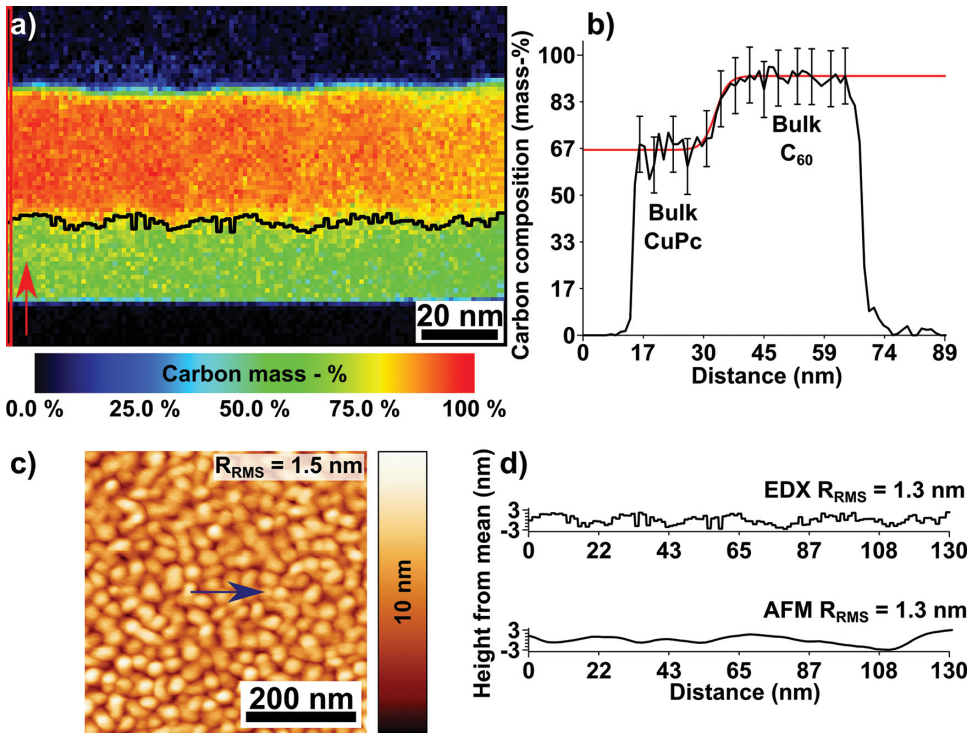

Figure 7. a) Quantitative carbon composition map obtained by EDX, with the black line representing the interface (see text). The red box was used to generate the composition profile (b) in the direction indicated by the arrow. b) Composition profile with the red line showing the fitted hyperbolic tangent function used to identify the slope midpoint. c) AFM image of a CuPc film grown under identical conditions to the corresponding film in the solar cell structure examined by EDX. d) Comparison of a CuPc topography profile (from the arrow in the AFM) and that of the interface roughness over an identical distance.

$$\frac{C_A}{C_B} = k_{AB}\frac{I_A}{I_B} \quad (1)$$

C_A and C_B are the compositions (in mass-%) of elements A and B in the specimen, I_A and I_B are the X-ray intensities emitted from elements A and B, and the Cliff-Lorimer k-factor, k_{AB}, is a sensitivity factor describing the relationship between composition and the measured X-ray intensities. Theoretical k-factors can be calculated from first principles but they include experimental and theoretical parameters, many of which are poorly defined. The result is that the error on these theoretical k-factors can be as high as ±20% (relative) and should be used with appropriate caution.[67] Therefore, any application of the Cliff-Lorimer method requires careful analysis of the quantification errors.

Using theoretical k-factors a STEM-EDX spectrum image data set obtained from a CuPc/C_{60} bi-layer on silicon was analysed to obtain chemical compositions. In the CuPc film, mass ratios of 1:0.27:0.09 for C, N and Cu respectively were obtained, which compare favourably to 1:0.29:0.17 from the known molecular composition. As the discrepancies are likely due to errors in the theoretical k-factor we use our knowledge of the CuPc molecular stoichiometry to derive experimental k-factors that will provide a higher accuracy for the calculation of the error in the composition. This yields mass-% values for C, N and Cu of 63.4 ± 10.0, 17.1 ± 4.2 and 5.42 ± 1.8. Note that the total does not sum to 100% due to the contribution of signals from oxygen and silicon. The amounts of oxygen and silicon vary around 9–6% and 3–6% respectively in the films, with the highest silicon mass-% found close to the substrate and higher oxygen content in the CuPc layer. Although the errors above are calculated from data located in the CuPc region, the error for the carbon composition should be similar in the C_{60} region since the experimental conditions for acquiring the spectra are the same, carbon is the main elemental component and the foil thickness is unchanged.

A quantified spectrum image detailing the carbon composition of the bi-layer structure is displayed in **Figure 7**a. A composition profile, with a width of 1.2 nm, extracted from the region highlighted in red on the map is shown in Figure 7b. In this profile the regions corresponding to the CuPc and C_{60} films can be identified. The slope of the composition profile at the interface between these two films is influenced by the spatial resolution of the STEM-EDX method as well as the boundary morphology at the interface. The abruptness of the profile at the Si/CuPc interface suggests that the STEM-EDX spatial resolution is not the limiting factor. Since the change in composition between the regions is larger than the error calculated for the carbon composition the profile can be used to define the position of the interface.

Assuming that the midpoint of the slope represents the interface position in the profile, plotting this as a function of horizontal distance can define the interface. This was accomplished by extracting similar profiles to that of Figure 7b across the width of the heterostructure in Figure 7a. A hyperbolic tangent function, Equation (2), which describes the shape of the profile over the bulk regions and the interface, was fitted to the carbon mass-% over all profiles. The overlaid red line in Figure 7b shows the function fitted to the profile.

$$y = A + B\tanh\left(\frac{x - C}{D}\right) \quad (2)$$

Where C is the slope midpoint, D represents the width of the slope, and A and B are its offset and amplitude respectively. The resulting interface, corresponding to the position of C, is plotted as a black line in Figure 7a. The observed roughness of this interface is quantified by extracting a root mean square value (R_{RMS}) of 1.3 nm. Despite the small sampling volume of the STEM-EDX method this value correlates well with the roughness extracted from a topography map obtained using atomic force microscopy (AFM), which yields an R_{RMS} of 1.5 nm for the total map region, and 1.3 nm from a profile over a distance equal to that of the EDX map (Figure 7c and d).

3. Conclusions

It has been shown that CuPc and C_{60} films in typical solar cell structures can be prepared using the in situ lift-out method with a focused beam of gallium ions and imaged using HRTEM whilst retaining their crystalline nature. During sample preparation it is important to reduce the energy transfer perpendicular to the foil. This is accomplished by reducing the accelerating voltage, beam current and the angle which the beam makes with the lamella.

Lattice fringes are found in both the CuPc and C_{60} films in solar cell structures grown on silicon. The orientation of these fringes allows conclusions about molecular orientations to be drawn. It is also shown that the crystallinity of C_{60} films is dependent on the nature of the surface on which they are grown.

Device structures grown on ITO glass show an increase in complexity attributed to the rougher substrate. For the case of the bi-layer and templated bi-layer structures, fringes are observed which can be correlated with the structures grown on silicon. The bulk-heterojunction structure displays very few fringes with the only ones observed found in the pure C_{60} film.

In an effort to define interface position in a simple bi-layer heterostructure, we have developed a novel method using STEM-EDX spectrum imaging to identify the organic-organic interface using the change in carbon composition between CuPc and C_{60}. The interface roughness obtained using this procedure correlates well with the roughness of the bottom molecular layer, as determined by AFM.

Our methodology could be extended to the study of any complex organic device structures, including those with amorphous materials, and will hopefully provide key insight into the role of the buried structure in organic electronics.

4. Experimental Section

4.1. Thin Film Growth

All films were grown in a Kurt J. Lesker SPECTROS high vacuum chamber with a base pressure of 10^{-7} mbar. For all organic films the growth rate was set at 1 Ås^{-1} and the thickness monitored using a quartz crystal micro balance. The aluminium film was grown in two stages; with 20 nm deposited using a rate of 0.2 Ås^{-1} and 80 nm deposited using a rate of 0.5 Ås^{-1}. Commercially available substrates (Si <100>, Virginia semiconductor) and ITO glass (Psiotec) were sonicated for 10 minutes in acetone and then IPA before being dried using pressurised air and placed in the vacuum chamber. Powders of CuPc (Sigma-Aldrich, twice purified using gradient sublimation), C_{60} (99%, Alfa Aesar), BCP (Sigma-Aldrich), PTCDA (Sigma-Aldrich) and aluminium (Sigma-Aldrich) were used to grow the films.

Table 1. Parameters used for thinning crude lamellas to electron transparency.

Lamella thickness [nm]	Accelerating voltage [kV]	Beam current [pA]	Φ [°]	Milling pattern
~1000	30	93	±1	CCS
~300	5	16	±0.5	CCS
~100	2	10	±0.2	CCS
~60	1	5.3	±0.2	Rectangle

4.2. Sample Cross-Sectioning

Cross-sectional samples of the solar cell structures were prepared using an FEI Helios NanoLab 600 system, incorporating a platinum gas injection system. A 2.3 µm thick platinum strip was deposited, the initial 100 nm of which occurred via e-beam deposition, with the remaining thickness deposited using the ion-beam. Crude milling of the lamella subsequently followed. For samples grown on silicon, the lamella was milled to be parallel to a Si [110] cleaved edge. After extraction and attachment to a TEM grid (Omniprobe) thinning commenced using parameters presented in **Table 1**.

Detailed descriptions of the milling patterns can be found in the paper by Schaffer et al.[48] The key feature of our methodology has been to reduce the energy transfer perpendicular to the lamella. This is accomplished by reducing the three parameters of accelerating voltage, beam current and angle which the beam makes with the lamella (denoted Φ in the table). A schematic of how this energy transfer is affected by the change in this angle can be found in **Figure 8**.

The success rate of the technique is very high, with failure occurring solely at the lift-out stage of the preparation procedure.

4.3. HRTEM Imaging

All HRTEM imaging was performed on a Cs corrected FEI Titan 80–300 equipped with a field emission gun (FEG) operated at 300 kV. The image displayed in Figure 2 was formed using a 20 µm objective aperture which prevents spatial information below ~0.3 nm from forming the image. For all other images no objective aperture was used. Images were acquired on a CCD camera using doses between 3 and 5 Ccm^{-2} and acquisition

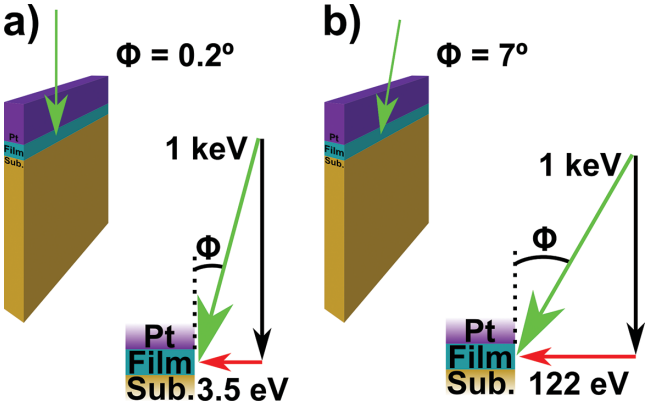

Figure 8. Schematics highlighting the effect that the beam-lamella angle has on the energy transfer perpendicular to the TEM foil. An angle of 0.2° (a) is used in this work, where 7° (b) is used in other works.

times of between 0.175 and 0.25 s. For the structures grown on silicon substrates, the foil was tilted to the Si [110] zone-axis. This ensures that the substrate surface and therefore any subsequent interface, is parallel to the electron beam, minimizing information projection.

Typically, from one cross-section 8 to 18 HRTEM images can be taken, each over an un-exposed region of the organic film. Care must be taken to avoid unnecessary exposure of the organic film by blanking the beam while moving to a fresh region. In total, eight foils of the bi-layer on silicon structure have been prepared and analysed using HRTEM. In all eight foils the structure described here has been observed, demonstrating the reproducibility of the technique. For the other five device structures two cross-section of each were prepared and analysed using HRTEM, all displaying the structures described.

FFTs of the images were calculated using Gatan's Digital Micrograph software. The images displayed in Figure 4b, c and d and S2 a and b were made by isolating the frequencies between 1.25 – 1.95 nm^{-1}, at an angular range over 60° parallel to the substrate surface i.e. the CuPc (100) lattice frequencies, performing the inverse FFT, and the overlaying the result on the original image. Averaging FFTs of multiple images was performed using the median blend tool in GNU Image Manipulation Program's G'MIC filter.

4.4. STEM-EDX

EDX spectra were collected using an FEI ChemiSTEM Titan^3 60–300 equipped with a FEG (X-FEG) operated at 300 kV in STEM mode. EDX acquisition was performed using a windowless silicon drift detector using Esprit 1.9 software from Bruker. Bremsstrahlung continuum removal and quantification of EDX spectra was also performed in Esprit 1.9. Gaussian curves were fitted to the carbon, nitrogen and copper Kα emission lines in X-ray spectra from only the CuPc region using the multiple peak fit tool in Origin 9.0 by OriginLab. The square root of integrated area of the fitted carbon, nitrogen and copper X-ray lines was used as the intensity component in calculating the error, i.e. a 68.2% confidence. Hyperbolic tangent functions were fitted to composition profiles using a least mean squares fitting routine in Matlab 2013b by MathWorks. Similar to bright field imaging, the specimen was tilted to the Si [110] zone-axis.

4.5. AFM

AFM measurements were conducted in air using a Dimension 3100 AFM with Nanoscope V controller and operated in tapping mode using silicon cantilevers (MikroMasch), and the images were processed using the WSxM software.[68]

Supporting Information

Supporting Information is available from the Wiley Online Library or from the author.

Acknowledgements

JBG thanks the Engineering and Physical Sciences Research Council for the award of a Doctoral Training Account, and the Fraser group for hosting the visit to Ohio. SCC thanks the National Research Foundation (NRF) Singapore and the National University of Singapore Graduate School for Integrative Sciences and Engineering (NGS) for financial support. DWM acknowledges support from The Ohio Third Frontier Program through an Ohio Research Scholar award.

Received: January 31, 2014
Revised: April 17, 2014
Published online: August 22, 2014

[1] B. A. Gregg, *J. Phys. Chem. B* **2003**, *107*, 4688.
[2] P. Peumans, S. Uchida, S. R. Forrest, *Nature* **2003**, *425*, 158.
[3] B. Kippelen, J.-L. Brédas, *Energy Environ. Sci.* **2009**, *2*, 251.
[4] T. Ameri, P. Khoram, J. Min, C. J. Brabec, *Adv. Mater.* **2013**, *25*, 4245.
[5] P. Peumans, V. Bulović, S. R. Forrest, *Appl. Phys. Lett.* **2000**, *76*, 2650.
[6] Z. Wu, T. Song, Y. Jin, B. Sun, *Appl. Phys. Lett.* **2011**, *99*, 143306.
[7] W. Li, K. H. Hendriks, W. S. C. Roelofs, Y. Kim, M. M. Wienk, R. A. J. Janssen, *Adv. Mater.* **2013**, *25*, 3182.
[8] J. J. M. Halls, C. A. Walsh, N. C. Greenham, E. A. Marseglia, R. H. Friend, S. C. Moratti, A. B. Holmes, *Nature* **1995**, *376*, 498.
[9] R. F. Service, *Science* **2011**, *332*, 293.
[10] S. Lizin, S. Van Passel, E. De Schepper, L. Vranken, *Sol. Energy Mater. Sol. Cells* **2012**, *103*, 1.
[11] M. Riede, T. Mueller, W. Tress, R. Schueppel, K. Leo, *Nanotechnology* **2008**, *19*, 424001.
[12] Y. Sun, G. C. Welch, W. L. Leong, C. J. Takacs, G. C. Bazan, A. J. Heeger, *Nat. Mater.* **2012**, *11*, 44.
[13] H. Bronstein, Z. Chen, R. S. Ashraf, W. Zhang, J. Du, J. R. Durrant, P. S. Tuladhar, K. Song, S. E. Watkins, Y. Geerts, M. M. Wienk, R. A. J. Janssen, T. D. Anthopoulos, H. Sirringhaus, M. Heeney, I. McCulloch, *J. Am. Chem. Soc.* **2011**, *133*, 3272.
[14] Y. Lin, Y. Li, X. Zhan, *Chem. Soc. Rev.* **2012**, *41*, 4245.
[15] B. P. Rand, D. Cheyns, K. Vasseur, N. C. Giebink, S. Mothy, Y. Yi, V. Coropceanu, D. Beljonne, J. Cornil, J.-L. Brédas, J. Genoe, *Adv. Funct. Mater.* **2012**, *22*, 2987.
[16] P. Sullivan, T. S. Jones, A. J. Ferguson, S. Heutz, *Appl. Phys. Lett.* **2007**, *91*, 233114.
[17] J. Cabanillas-Gonzalez, M. Schmidt, O. Peña-Rodríguez, M. I. Alonso, A. R. Goñi, M. Campoy-Quiles, *J. Nanosci. Nanotechnol.* **2013**, *13*, 5148.
[18] W. Ma, J. R. Tumbleston, M. Wang, E. Gann, F. Huang, H. Ade, *Adv. Energy Mater.* **2013**, *3*, 864.
[19] D. Chen, F. Liu, C. Wang, A. Nakahara, T. P. Russell, *Nano Lett.* **2011**, *11*, 2071.
[20] J. R. Tumbleston, B. A. Collins, L. Yang, A. C. Stuart, E. Gann, W. Ma, W. You, H. Ade, *Nat. Photonics* **2014**, *8*, 385.
[21] H. Yan, S. Swaraj, C. Wang, I. Hwang, N. C. Greenham, C. Groves, H. Ade, C. R. McNeill, *Adv. Funct. Mater.* **2010**, *20*, 4329.
[22] W. Yin, M. Dadmun, *ACS Nano* **2011**, *5*, 4756.
[23] K. H. Lee, Y. Zhang, P. L. Burn, I. R. Gentle, M. James, A. Nelson, P. Meredith, *J. Mater. Chem. C* **2013**, *1*, 2593.
[24] T. Mönch, P. Guttmann, J. Murawski, C. Elschner, M. Riede, L. Müller-Meskamp, K. Leo, *Org. Electron.* **2013**, *14*, 2777.
[25] R. Saive, M. Scherer, C. Mueller, D. Daume, J. Schinke, M. Kroeger, W. Kowalsky, *Adv. Funct. Mater.* **2013**, *23*, 5854.
[26] S. W. Cho, A. DeMasi, A. R. H. Preston, K. E. Smith, L. F. J. Piper, K. V. Chauhan, T. S. Jones, *Appl. Phys. Lett.* **2012**, *100*, 263302.
[27] P. Westacott, J. R. Tumbleston, S. Shoaee, S. Fearn, J. H. Bannock, J. B. Gilchrist, S. Heutz, J. DeMello, M. Heeney, H. Ade, J. R. Durrant, D. S. McPhail, N. Stingelin, *Energy Environ. Sci.* **2013**, *6*, 2756.
[28] T. Kobayashi, S. Isoda, *J. Mater. Chem.* **1993**, *3*, 1.
[29] J. B. Gilchrist, S. Heutz, D. W. McComb, *J. Phys. Conf. Ser.* **2012**, *371*, 012042.
[30] C. Vergnat, V. Landais, J.-F. Legrand, M. Brinkmann, *Macromolecules* **2011**, *44*, 3817.
[31] J. R. Fryer, *J. Phys. D. Appl. Phys.* **1993**, *26*, B137.
[32] M. Haruta, H. Kurata, *Sci. Rep.* **2012**, *2*, 252.
[33] M. Haruta, K. Yoshida, H. Kurata, S. Isoda, *Ultramicroscopy* **2008**, *108*, 545.
[34] V. Jantou, M. Turmaine, G. D. West, M. A. Horton, D. W. McComb, *Micron* **2009**, *40*, 495.
[35] A. C. Dürr, F. Schreiber, M. Kelsch, H. Dosch, *Ultramicroscopy* **2003**, *98*, 51.

[36] M. Lekstrom, M. A. McLachlan, S. Husain, D. W. McComb, B. A. Shollock, *J. Phys. Conf. Ser.* **2008**, *126*, 012028.
[37] S. Kim, M. Jeong Park, N. P. Balsara, G. Liu, A. M. Minor, *Ultramicroscopy* **2011**, *111*, 191.
[38] J. Mayer, L. A. Giannuzzi, T. Kamino, J. Michael, *MRS Bull.* **2011**, *32*, 400.
[39] Y. Yabuuchi, *J. Electron Microsc. (Tokyo)*. **2004**, *53*, 471.
[40] S. D. Oosterhout, M. M. Wienk, S. S. van Bavel, R. Thiedmann, L. J. A. Koster, J. Gilot, J. Loos, V. Schmidt, R. A. J. Janssen, *Nat. Mater.* **2009**, *8*, 818.
[41] B. V. Andersson, A. Herland, S. Masich, O. Inganäs, *Nano Lett.* **2009**, *9*, 853.
[42] S. Heutz, R. Cloots, T. S. Jones, *Appl. Phys. Lett.* **2000**, *77*, 3938.
[43] S. M. Schultes, P. Sullivan, S. Heutz, B. M. Sanderson, T. S. Jones, *Mater. Sci. Eng. C* **2005**, *25*, 858.
[44] T. Ichihashi, K. Tanigaki, T. W. Ebbesen, S. Kuroshima, S. Iijima, *Chem. Phys. Lett.* **1992**, *190*, 179.
[45] H. Tanimoto, K. Yamada, H. Mizubayashi, Y. Matsumoto, H. Naramaoto, S. Sakai, *Appl. Phys. Lett.* **2008**, *93*, 151919.
[46] W. Zhao, W.-L. Zhou, L.-Q. Chen, Y.-Z. Huang, Z.-B. Zhang, K. K. Fung, Z.-X. Zhao, *J. Solid State Chem.* **1994**, *112*, 412.
[47] L. J. Allen, A. J. D'Alfonso, B. H. Freitag, D. O. Klenov, *MRS Bull.* **2012**, *37*, 47.
[48] M. Schaffer, B. Schaffer, Q. Ramasse, *Ultramicroscopy* **2012**, *114*, 62.
[49] S. Heutz, P. Sullivan, B. M. Sanderson, S. M. Schultes, T. S. Jones, *Sol. Energy Mater. Sol. Cells* **2004**, *83*, 229.
[50] A. Hoshino, Y. Takenaka, H. Miyaji, *Acta Crystallogr. Sect. B Struct. Sci.* **2003**, *59*, 393.
[51] M. Warner, S. Mauthoor, S. Felton, W. Wu, J. A. Gardener, S. Din, D. Klose, G. W. Morley, A. M. Stoneham, A. J. Fisher, G. Aeppli, C. W. M. Kay, S. Heutz, *ACS Nano* **2012**, *6*, 10808.
[52] T. Kobayashi, Y. Fujiyoshi, N. Uyeda, *Acta Crystallogr. Sect. A* **1982**, *38*, 356.
[53] Y. Murata, J. R. Fryer, T. Baird, H. Murata, *Acta Crystallogr. Sect. A* **1977**, *33*, 198.
[54] T. Kobayashi, K. Yase, N. Uyeda, *Acta Crystallogr. Sect. B Struct. Sci.* **1984**, *40*, 263.
[55] J. Gardener, J. H. G. Owen, K. Miki, S. Heutz, *Surf. Sci.* **2008**, *602*, 843.
[56] P. Gasser, U. E. Klotz, F. A. Khalid, O. Beffort, *Microsc. Microanal.* **2004**, *10*, 311.
[57] T. Ishitani, K. Umemura, T. Ohnishi, T. Yaguchi, T. Kamino, *J. Electron Microsc.* **2004**, *53*, 443.
[58] E. Montoya, S. Bals, M. D. Rossell, D. Schryvers, G. Van Tendeloo, *Microsc. Res. Tech.* **2007**, *70*, 1060.
[59] S. Rubanov, P. R. Munroe, *Micron* **2004**, *35*, 549.
[60] D. L. Dorset, M. P. McCourt, *Acta Crystallogr. Sect. A Found. Crystallogr.* **1994**, *50*, 344.
[61] V. P. Dravid, S. Liu, M. M. Kappes, *Chem. Phys. Lett.* **1991**, *185*, 75.
[62] Y. Jin, R. J. Curry, J. Sloan, R. A. Hatton, L. C. Chong, N. Blanchard, V. Stolojan, H. W. Kroto, S. R. P. Silva, *J. Mater. Chem.* **2006**, *16*, 3715.
[63] S. Heutz, T. S. Jones, *J. Appl. Phys.* **2002**, *92*, 3039.
[64] W. Wu, L. A. Rochford, S. Felton, Z. Wu, J. L. Yang, S. Heutz, G. Aeppli, T. S. Jones, N. M. Harrison, A. J. Fisher, *J. Appl. Phys.* **2013**, *113*, 013914.
[65] K. Tojo, J. Mizuguchi, *Zeitschrift für Krist.* **2002**, *217*, 255.
[66] D. B. Williams, C. B. Carter, *Transmission Electron Microscopy*, 2nd ed., Springer US, Boston, MA, **1996**; pp. 640.
[67] D. B. Williams, C. B. Carter, *Transmission Electron Microscopy*, 2nd ed., Springer US, Boston, MA, **1996**; p. 650.
[68] I. Horcas, R. Fernández, J. M. Gómez-Rodríguez, J. Colchero, J. Gómez-Herrero, A. M. Baro, *Rev. Sci. Instrum.* **2007**, *78*, 013705.